

Coronavirus rotational diffusivity

Cite as: Phys. Fluids 32, 113101 (2020); doi: 10.1063/5.0031875

Submitted: 4 October 2020 • Accepted: 12 October 2020 •

Published Online: 2 November 2020



M. A. Kanso,¹  J. H. Piette,¹  J. A. Hanna,² and A. J. Giacomin^{1,2,3,4,a)} 

AFFILIATIONS

¹Chemical Engineering Department, Polymers Research Group, Kingston, Ontario K7L 3N6, Canada

²Mechanical Engineering Department, University of Nevada, Reno, Nevada 89557-0312, USA

³Physics, Engineering Physics and Astronomy Department, Queen's University, Kingston, Ontario K7L 3N6, Canada

⁴Mechanical and Materials Engineering Department, Kingston, Ontario K7L 3N6, Canada

Note: This paper is part of the Special Topic, Flow and the Virus.

a) Author to whom correspondence should be addressed: giacomin@queensu.ca

ABSTRACT

Just 11 weeks after the confirmation of first infection, one team had already discovered and published [D. Wrapp *et al.*, “Cryo-EM structure of the 2019-nCoV spike in the prefusion conformation,” *Science* **367**(6483), 1260–1263 (2020)] in exquisite detail about the new coronavirus, along with how it differs from previous viruses. We call the virus particle causing the COVID-19 disease SARS-CoV-2, a spherical capsid covered with spikes termed *peplomers*. Since the virus is not motile, it relies on its own random thermal motion, specifically the rotational component of this thermal motion, to align its peplomers with targets. The governing transport property for the virus to attack successfully is thus the rotational diffusivity. Too little rotational diffusivity and too few alignments are produced to properly infect. Too much, and the alignment intervals will be too short to properly infect, and the peplomer is wasted. In this paper, we calculate the rotational diffusivity along with the complex viscosity of four classes of virus particles of ascending geometric complexity: tobacco mosaic, gemini, adeno, and corona. The gemini and adeno viruses share icosahedral bead arrangements, and for the corona virus, we use polyhedral solutions to the Thomson problem to arrange its peplomers. We employ general rigid bead–rod theory to calculate complex viscosities and rotational diffusivities, from first principles, of the virus suspensions. We find that our *ab initio* calculations agree with the observed complex viscosity of the tobacco mosaic virus suspension. From our analysis of the gemini virus suspension, we learn that the fine detail of the virus structure governs its rotational diffusivity. We find the characteristic time for the adenovirus from general rigid bead–rod theory. Finally, from our analysis of the coronavirus suspension, we learn that its rotational diffusivity descends monotonically with its number of peplomers.

Published under license by AIP Publishing. <https://doi.org/10.1063/5.0031875>

I. INTRODUCTION

Shortly after the confirmation of first infection, one team had already discovered and published¹ in exquisite detail about the new coronavirus, along with how it differs from previous viruses. We call the virus particle causing the COVID-19 disease SARS-CoV-2, a spherical capsid covered with hollow spikes termed *peplomers*. Since the virus is not motile, it relies on its own random thermal motion, specifically, the rotational component of this thermal motion, to align its peplomers with targets. From Fig. 1(B) of Ref. 2, we learn that to perfuse capsid contents into a cell, precisely two adjacent peplomers must align with a dimeric target, nominally rectangular ($110 \times 160 \text{ \AA}^2$). Furthermore, this alignment must be long enough for fusion. Once fused, perfusion progresses to infection.

Whereas much of the prior work on flow and the virus focuses on infection of the organism,^{3–21} this work targets the transport properties of the coronavirus particle and their implications in transport phenomena of cellular infection. Although our work is mainly driven by curiosity, it may deepen our understanding or even accelerate drug treatment or vaccine development, especially where these interfere with cellular infection.

The governing transport property for the virus to attack successfully is the rotational diffusivity of the SARS-CoV-2 particle (see Footnote 2 in p. 62 of Ref. 22). Too much rotational diffusivity and the alignment intervals will be too short to properly infect, and the peplomer is wasted. Too little rotational diffusivity, and too few alignments are produced to properly infect. The rotational diffusivity of a particle depends intimately on its shape.

Whereas in engineering, the complex viscosity function has a broad diversity of applications including polymer or suspension processing, for virus suspensions, its main use is for determining rotational diffusivity. In this paper, we calculate the complex viscosity and thus the rotational diffusivity of four classes of virus particles of ascending geometric complexity: tobacco mosaic, gemini, adeno, and corona. The gemini²³ and adeno²⁴ viruses share icosahedral bead arrangements, and for the corona virus, we use polyhedral solutions to the Thomson problem to arrange its peplomers.^{25,26} We employ general rigid bead–rod theory to calculate complex viscosities and rotational diffusivities, from first principles, of the virus suspensions (Refs. 27–34; see EXAMPLE 16.7-1 of Ref. 22 or EXAMPLE 13.6-1 of Ref. 35).

We are attracted to general rigid bead–rod theory first for its flexibility. We design each macromolecular structure, here virus particles, by rigidly connecting nearest bead centers with massless dimensionless rods. We are attracted to general rigid bead–rod theory second for the accuracy of its simplest special cases, the rigid dumbbell suspensions, for which many transport properties are predicted (see this reviewed in Sec. I of Ref. 31).

General rigid bead–rod theory proceeds from the continuity equation for the macromolecular configuration, called the *diffusion equation* [Eq. (13.2-13) of Ref. 22]. By *continuity*, we mean that the diffusion equation conserves orientation, preserving one and only one orientation per macromolecule. Hassager solves the diffusion equation for the configuration distribution function in small-amplitude oscillatory flows, which, for rigid macromolecules, reduces to the orientation distribution function, $\psi(\theta, \phi, t)$.

Consider, for instance, a coronavirus particle close enough to fuse with a dimeric receptor.² We refer the coronavirus particle to spherical coordinates and consider the receptor target orthogonal to its equator ($\theta = \pi/2$) with the long axis of the dimeric receptor along the longitudinal direction. For this special infection opportunity, the probability of finding a peplomer aligned with said receptor is given by [see Eq. (9) of Ref. 36]

$$p \equiv \int_{-\phi_r}^{\phi_r} \int_{-\theta_r}^{\theta_r} \psi(\theta, \phi, t) \sin \theta d\theta d\phi, \quad (1)$$

where for the nominally rectangular binding target,

$$\frac{\theta_r}{\phi_r} = \frac{110 \text{ \AA}}{160 \text{ \AA}} = \frac{11}{16}. \quad (2)$$

For fusion, we, of course, require two peplomers with said alignment,² and thus, the probability of finding this falls well below p .

General rigid bead–rod theory connects ψ with macromolecular shapes, including those of viruses. In this way, the virus shape confers the transport properties to its suspension, including viscosity, elasticity, and diffusivities, be they rotational or translational. Little is known experimentally about the diffusivity of viruses, especially the rotational diffusivity. For instance, the translational diffusivity of the adenovirus has been measured by photon-correlation spectroscopy.³⁷ The rotational diffusivity of tobacco mosaic viruses has also been measured by light scattering,^{38–41} transient electric birefringence,⁴² and flow birefringence.⁴³ The rotational diffusivity is deducible from the translational one by the identity given in Sec. II below.

One of the challenges of *ab initio* calculations from general rigid bead–rod theory on coronaviruses is that the peplomer arrangement is not known. However, we do know that the spikes are charge-rich,^{44,45} and we can presume, charged identically. Furthermore, we know that the coronavirus spikes are anchored into its viral membrane and not into its capsid (Sec. 1. of Ref. 46), unlike the adenovirus spikes. Hence, the coronavirus spikes are free to be rearranged by their electrostatic repulsions. We thus expect the peplomers to arrange themselves by repelling one another into the polyhedral solutions to the Thomson problem.^{25,26} By the *Thomson problem*, we mean how identically charged particles will organize themselves onto a sphere by minimizing system potential energy. In this work, we are thus using minimum potential energy peplomer arrangements for our coronavirus model particles.

The rotational alignment of the virus particle studied herein is prefusion and not to be confused with the postfusion *diffusive rotational search* of the spike-protein unfolding that accompanies binding.⁴⁷

II. METHOD

Using general rigid bead–rod theory, we propose the construction of virus particles from sets of beads whose positions are fixed relative to one another. For example, the SARS-CoV-2 particle geometry is a spherical capsid surrounded by a constellation of protruding peplomers. We understand that the number of peplomers per virus particle differs from particle to particle and seems to decrease with time after inoculation. We suspend our bead–rod models of virus particles into a Newtonian solvent. We begin by neglecting interactions of the solvent velocity fields, be they (i) between nearest beads within the virus particle^{48,49} or (ii) between nearest virus particles. To any such collection of bead masses, we can associate a *moment of inertia ellipsoid* (MIE) whose center is the center of mass and whose principal moments of inertia match those of the virus particle. The MIE thus determines the orientability of the virus particle and thus the virus rotational diffusivity. Our use of moment of inertia ellipsoids is not to be confused with replacing the virus particle with an ellipsoid of revolution, with its own hydrodynamic environment.⁵⁰ We know of no previous calculation of the moments of inertia ellipsoid of virus particles, and we think that this missing physics can deepen our understanding of SARS-CoV-2.

To model the virus particle, we locate each bead of mass m_i with the position vector of the i th bead \mathbf{r}_i , where the virus particle center of mass \mathbf{R} satisfies

$$\sum_{i=1}^N m_i (\mathbf{r}_i - \mathbf{R}) = 0 \quad (3)$$

so that

$$\mathbf{R} = \frac{1}{M} \sum_{i=1}^N m_i \mathbf{r}_i, \quad (4)$$

where N is the total number of beads and $M \equiv \sum_{i=1}^N m_i$ is the virus particle mass. Since we construct our virus particles with identical beads of diameter d and mass m , then $M = mN$, and thus, the center

of mass is

$$\mathbf{R} = \frac{1}{N} \sum_{i=1}^N \mathbf{r}_i, \quad (5)$$

which we will use below.

We next install *viral coordinates* at the center of mass of the virus, and we orient these Cartesian coordinates such that $\hat{\delta}_3$ is along the polar axis of the *moment of inertia ellipsoid*. For our virus particles, $\hat{\delta}_3$ is through the particle. In this study, to allow us to explore the surface density of peplomers, the peplomer arrangement, and even the triadic details of the three-glycoprotein spikes, we will use a finely beaded sphere for the capsid. By necessity of general rigid bead-rod theory, our capsid and peplomer beading must be equally fine.

The position vector of the i th bead with respect to the virus center of mass is given by

$$\mathbf{R}_i \equiv [R_{i1}, R_{i2}, R_{i3}]. \quad (6)$$

We define the principal moments of inertia I_1 , I_2 , and I_3 by [Eqs. (16.7-17) and (16.7-18) of Ref. 22 or (13.6-17) and (13.6-18) of Ref. 35]

$$I_1 \equiv m \sum_{i=1}^N (R_{i2}^2 + R_{i3}^2), \quad (7)$$

$$I_2 \equiv m \sum_{i=1}^N (R_{i1}^2 + R_{i3}^2), \quad (8)$$

$$I_3 \equiv 2m \sum_{i=1}^N R_{i1}^2, \quad (9)$$

where the subscript i is the bead number. We design each virus particle structure by first rigidly connecting nearest bead centers with massless widthless rods. Throughout our work, L is the distance between the nearest bead centers. We then complete the general rigid bead-rod construction by rigidly connecting the remaining bead centers to their nearest neighbors. For the SARS-CoV-2 particle, L is the center to center distance between osculating beads forming the capsid. Although the peplomer is a spike with a bulbous triadic head, in this work, we will model it as a single bead not touching the capsid.

Since the virus particle structure is axisymmetric, so will be its moment of inertia ellipsoid. By *axisymmetric*, we mean that both the virus particle and its moment of inertia ellipsoid have at least one axis of symmetry.²⁷ Furthermore, if the virus particle structure is axisymmetric, at least two of its principal moments of inertia equate, at any angle from the molecular axis, so that $I_1 = I_2$. Our usage of *axisymmetric* is not to be confused with the common geometric meaning of continuous rotational symmetry about an axis.

Hassager derives the expression for the dimensionless shear relaxation function for general rigid bead-rod theory,

$$\frac{G(s)}{nkT} = \frac{\delta(s)}{kT} \left(\frac{2\eta_s}{n} + \zeta L^2 a \right) + b e^{-s/\lambda}, \quad (10)$$

in which [Eq. (16.7-38) of Ref. 22 or Eqs. (13.6-44), (13.6-45), and (13.6-46) of Ref. 35]

$$a \equiv \frac{2I_1 + I_3}{6mL^2} - \frac{(I_1 - I_3)^2}{5mL^2 I_1}, \quad (11)$$

$$b \equiv \frac{3(I_1 - I_3)^2}{5I_1^2} \quad (12)$$

and the particle rotation constant is^{29,31}

$$v \equiv \frac{6mL^2}{I_1}, \quad (13)$$

where $0 \leq b \leq 3/5$ and $0 \leq av \leq 7/2$. The three quantities a , b , and v thus define completely the differences in linear viscoelastic behaviors arising between different axisymmetric macromolecular structures. Whereas we associate a with the Dirac delta function contribution to the relaxation function, we associate b with the dying exponential.

The relaxation time of the corresponding virus particle suspension can be expressed as

$$\lambda \equiv \frac{\zeta I_1}{6mkT} \equiv \frac{\zeta L^2}{vkT} \quad (14)$$

in which the bead friction coefficient is given by

$$\zeta \equiv 3\pi d\eta_s. \quad (15)$$

We define a characteristic time for all virus particle suspensions as

$$\lambda_0 \equiv \frac{\zeta L^2}{12kT} = \frac{\pi d\eta_s L^2}{4kT}, \quad (16)$$

which nondimensionalizes as

$$\frac{nkT\lambda_0}{\eta_s} \equiv \frac{3}{4}\varphi \left(\frac{L}{d} \right)^2, \quad (17)$$

where φ is the bead volume fraction, and for osculating beads, where $L = d$,

$$\lambda_0 = \frac{\pi d^3 \eta_s}{4kT} \quad (18)$$

and

$$\frac{nkT\lambda_0}{\eta_s} \equiv \frac{3}{4}\varphi. \quad (19)$$

Dividing Eq. (14) by Eq. (16) normalizes the relaxation time,

$$\frac{\lambda}{\lambda_0} \equiv \frac{12}{v}. \quad (20)$$

We can then use Eq. (10) to calculate the polymer contribution to the stress tensor in any linear viscoelastic flow, including oscillatory shear flow, from [Eq. (1) of Ref. 30]

$$\tau_p \equiv - \int_{-\infty}^t G(t-t') \dot{\gamma}(t') dt', \quad (21)$$

where all symbols are defined in Tables I and II.

TABLE I. Dimensional variables $M \equiv$ mass, $L \equiv$ length, and $t \equiv$ time.

Name	Unit	Symbol
Angular frequency	t^{-1}	ω
Avogadro constant	mol^{-1}	\tilde{N}
Bead diameter	L	d
Bead friction coefficient [Eq. (15)]	M/t	ζ
Capsid radius (see Figs. 4 and 8)	L	r_c
Cartesian coordinates	L	x, y, z
Cartesian coordinates with respect to the center of mass	L	$\hat{\delta}_1, \hat{\delta}_2, \hat{\delta}_3$
Characteristic time for each virus particle suspension	s	λ_s
Characteristic time, zero-shear	t	λ_c
Complex viscosity [Eq. (36)]	M/Lt	η^*
Density	M/L^3	ρ
Edge vector pointing from adenovirus vertex i to vertex j	L	\mathbf{E}_{ij}
Element for Kronecker delta [Eq. (10)]	t^{-1}	$\delta(s)$
Energy values in molecular-scale systems	ML^2/t^2	kT
Intrinsic minus imaginary part of non-linear complex viscosity	L^3/M	$[\eta'']$
Intrinsic real part of non-linear complex viscosity	L^3/M	$[\eta']$
Intrinsic zero-shear viscosity	L^3/M	$[\eta]_0$
Macromolecular center of mass [Eq. (5)]	L	\mathbf{R}
Mass concentration	M/L^3	c
Mass of each bead	M	m_i
Minus imaginary part of non-linear complex viscosity [Eq. (35)]	M/Lt	η''
Moments of inertia [Eqs. (7)–(9)]	ML^2	I_1, I_2, I_3
Number of dumbbells per unit volume	$1/L^3$	n
Peplomer bulb center radial position (see Fig. 8)	L	$r_p \equiv r_v - r_b$
Peplomer bulb radius (see Fig. 8)	L	r_b
Polymer contribution to the stress tensor [Eqs. (21) and (33)]	M/Lt^2	τ_p
Position vector of the i th bead and j th element with respect to the center of mass [Eq. (6)]	L	R_{ij}
Position vector of the i th bead with respect to the center of mass [Eq. (6)]	L	\mathbf{R}_i
Position vector of the i th bead [Eq. (5)]	L	\mathbf{r}_i
Position vector of adenovirus vertex i with respect to the center of mass	L	\mathbf{V}_i
Real part of non-linear complex viscosity [Eq. (34)]	M/Lt	η'
Reduced angular frequency	M/L^3	ω_R
Relaxation time of rigid dumbbell [Eq. (16)]	t	λ_0
Relaxation time of solution Eq. (14)	t	λ
Rotational diffusivity	s^{-1}	D_r
Rotatory diffusivity	L^2/t	D_{rot}
Shear rate amplitude [Eq. (29)]	t^{-1}	$\dot{\gamma}^0$
Shear rate at specific time t' [Eq. (21)]	t^{-1}	$\dot{\gamma}(t')$
Shear rate tensor [Eq. (29)]	t^{-1}	$\dot{\boldsymbol{\gamma}}(t)$
Shear rate [Eq. (29)]	t^{-1}	$\dot{\gamma}(t)$
Shear relaxation function [Eq. (10)]	M/Lt^2	$G(s)$
Solvent viscosity	M/Lt	η_s
Specific time [Eq. (21)]	t	t'
Temperature	T	T
Time	t	t
Time difference	t	$s \equiv t - t'$
Total mass	M	M
Translational diffusivity	L^2/t	D_{tr}
Virus radius (see Figs. 4 and 8)	L	$r_v \equiv r_p + r_b$
Viscosity, zero-shear	M/Lt	η_0
Zero-shear first normal stress difference	M/L	$\Psi_{0,1}$

TABLE II. Dimensionless variables and groups.

Name	Symbol
Bead volume fraction [Eq. (17)]	φ
Coefficient in Eq. (11)	a
Coefficient in Eq. (12)	b
Coefficient in Eq. (13)	ν
Deborah number, oscillatory shear	$De \equiv \lambda\omega$
Golden Ratio	β
Relaxation time ratio	$\Lambda \equiv \lambda/\lambda_0$
Total number of beads	N
Total number of peplomers	N_p
Total number of capsid beads	N_c
Weissenberg number	$Wi \equiv \lambda\dot{\gamma}^0$
Probability	p
Orientation distribution	$\psi(\theta, \phi, t)$
Spherical coordinate, latitudinal	θ
Spherical coordinate, longitudinal	ϕ
Spherical coordinate, latitudinal receptor	θ_r
Spherical coordinate, longitudinal receptor	ϕ_r

In this work, we apply these derivations to virus particles, specifically to the calculation of the rotational diffusivity, given by the identity (see Footnote 2 of p. 62 of Ref. 22)

$$D_r \equiv \frac{1}{6\lambda} \tag{22}$$

about which, for virus particles, remarkably little is known. Substituting Eq. (20) into Eq. (22) and nondimensionalizing,


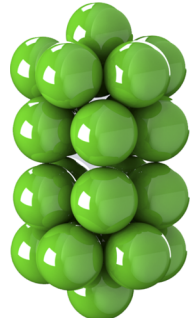
$$\lambda_0 D_r = \frac{\nu}{72}. \tag{23}$$

Substituting Eq. (17) into this and rearranging gives the *dimensionless rotational diffusivity*

$$\lambda_s D_r \equiv \frac{\eta_s}{nkT} D_r = \frac{\nu}{54\varphi} \left(\frac{d}{L}\right)^2 \tag{24}$$

from which we uncover a characteristic time for each virus particle suspension λ_s . The quantity ν thus defines completely the rotational diffusivity of a virus particle.

TABLE III. Bead positions for tobacco mosaic and gemini viruses.

Macromolecule	$L[R_{i1}, R_{i2}, R_{i3}]$
	$\left[0, 0, -\frac{11}{2}\right]; \left[0, 0, -\frac{9}{2}\right]; \left[0, 0, -\frac{7}{2}\right]; \left[0, 0, -\frac{5}{2}\right]; \left[0, 0, -\frac{3}{2}\right]; \left[0, 0, -\frac{1}{2}\right];$ $\left[0, 0, \frac{11}{2}\right]; \left[0, 0, \frac{9}{2}\right]; \left[0, 0, \frac{7}{2}\right]; \left[0, 0, \frac{5}{2}\right]; \left[0, 0, \frac{3}{2}\right]; \left[0, 0, \frac{1}{2}\right]$
	$\left[0, 0, x_1\right]; \left[-x_2, 0, \frac{1}{2}\right]; \left[x_2, 0, x_3\right]; \left[x_4, -\frac{1}{2}, \frac{1}{2}\right];$ $\left[x_4, \frac{1}{2}, \frac{1}{2}\right]; \left[-x_4, -\frac{1}{2}, x_3\right]; \left[-x_4, \frac{1}{2}, x_3\right];$ $\left[-x_5, -x_6, \frac{1}{2}\right]; \left[-x_5, x_6, \frac{1}{2}\right]; \left[x_5, -x_6, x_3\right];$ $\left[x_5, x_6, x_3\right]; \left[0, 0, -x_1\right]; \left[-x_2, 0, -\frac{1}{2}\right]; \left[x_2, 0, -x_3\right];$ $\left[x_4, -\frac{1}{2}, -\frac{1}{2}\right]; \left[x_4, \frac{1}{2}, -\frac{1}{2}\right]; \left[-x_4, -\frac{1}{2}, -x_3\right];$ $\left[-x_4, \frac{1}{2}, -x_3\right]; \left[-x_5, -x_6, -\frac{1}{2}\right]; \left[-x_5, x_6, -\frac{1}{2}\right];$ $\left[x_5, x_6, -x_3\right]; \left[x_5, x_6, -x_3\right]$ <p>where</p> $x_1 \equiv \frac{1}{2} + \frac{5}{\sqrt{50 - 10\sqrt{5}}} + \frac{1}{\sqrt{10 - 2\sqrt{5}}}, x_2 \equiv \sqrt{\frac{2}{5 - \sqrt{5}}},$ $x_3 \equiv \frac{1}{2} + \frac{2}{\sqrt{10 - 2\sqrt{5}}}, x_4 \equiv \frac{1}{2} \sqrt{\frac{5}{10 - 2\sqrt{5}}} + \frac{1}{2\sqrt{10 - 2\sqrt{5}}},$ $x_5 \equiv \frac{1}{2\sqrt{10 - 2\sqrt{5}}} - \frac{1}{2} \sqrt{\frac{5}{10 - 2\sqrt{5}}}, x_6 \equiv \frac{1}{2} \sqrt{\frac{5 + \sqrt{5}}{5 - \sqrt{5}}}$

In the tradition of the transport sciences, we define the *rotatory diffusivity* as (see Footnote 2 of p. 62 of Ref. 22)

$$D_{\text{rot}} \equiv \frac{2kT}{\zeta}, \quad (25)$$

which, for any axisymmetric macromolecule, from general rigid bead-rod theory, gives

$$D_{\text{rot}} \equiv \frac{12L^2}{\nu} D_r, \quad (26)$$

which has the dimensions of diffusivity and which is four times the *translational diffusivity*,

$$D_{\text{rot}} \equiv 4D_{tr} \quad (27)$$

or

$$D_r \equiv \frac{\nu}{3L^2} D_{tr}. \quad (28)$$

In this paper, we depart from said transport tradition of using the rotatory diffusivity, D_{rot} , and frame our results in terms of the rotational diffusivity, D_r .

The challenge in determining the rotational diffusivity of a virus particle, from first principles, begins with modeling its intricate geometry with beads, locating the position of each bead. Once overcome, the next challenge is to use this geometry to arrive at the transport properties for the SARS-CoV-2 particle. From these, we will deepen our understanding of how these remarkable particles can align their peplomers both for long enough and often enough to infect.

For this work, we chose general rigid bead-rod theory for its flexibility and accuracy (Sec. I of Ref. 31). However, for bead-rod structures as complex as coronaviruses, drawing the bead-rod models presented a challenge, which we met using solid modeling computer-aided design.⁵¹ This challenge arises when progressing from the \mathbf{R} values in Eq. (5) to bead-rod imagery, for instance, when going from Table III for the \mathbf{R} values of our tobacco mosaic and gemini viruses to our images in Figs. 1–5, respectively.

In Secs. IV–VII, we calculate the rotational diffusivity along with the complex viscosity of four classes of virus particles of ascending geometric complexity: tobacco mosaic, gemini, adeno, and corona. Section IV affords a comparison of our general bead-rod theory with measured behavior of the complex viscosity.

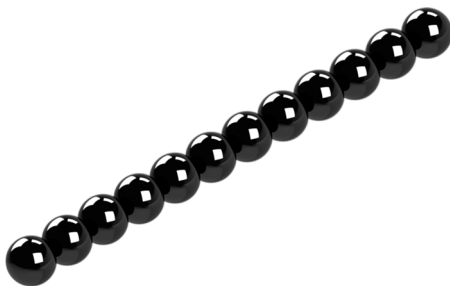


FIG. 1. General rigid bead-rod model of tobacco mosaic virus, $N = 12$.

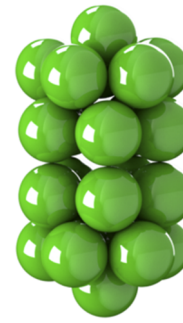


FIG. 2. General rigid bead-rod model of gemini virus, $N = 22$. See Fig. 2 of Ref. 23.

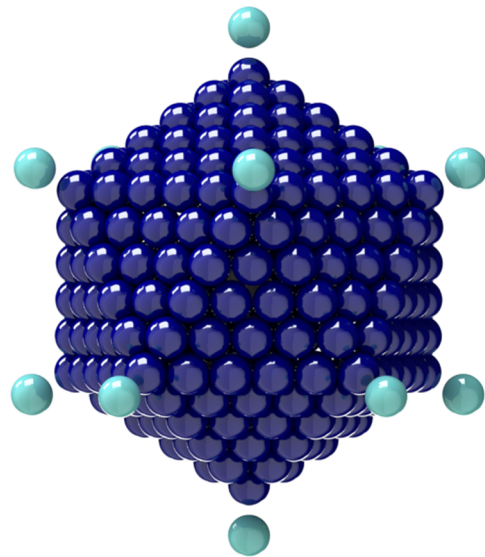


FIG. 3. General rigid bead-rod model of adenovirus, $N_c = 252$, $N_p = 12$, and $r_v/r_c = 5/4$.

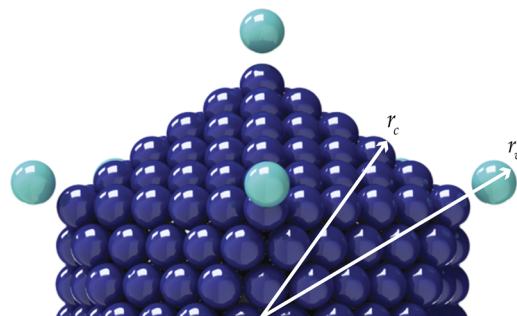


FIG. 4. Connections between adenovirus particle dimensions and its general rigid bead-rod model.

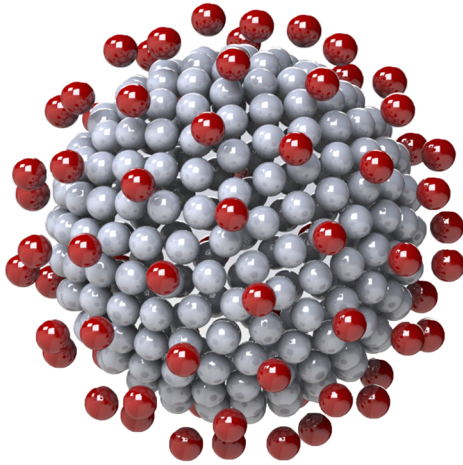


FIG. 5. General rigid bead–rod model of coronavirus, $N_c = 256$, $N_p = 74$, and $r_v/r_c = 5/4$.

Section V is purposed to explore how fine structural detail affects virus rotational diffusivity. Section VI affords a comparison with the measured value of the translational diffusivity, and Sec. VII, affords an exploration of how the detailed structure of SARS-CoV-2 affects its rotational diffusivity.

III. OSCILLATORY SHEAR FLOW

One measures the complex viscosity in oscillatory shear flow generated by confining the fluid to a simple shear apparatus and then by subjecting one solid–liquid boundary to a coplanar sinusoidal displacement, generating the corresponding cosinusoidal shear rate

$$\dot{\gamma}(t) = \dot{\gamma}^0 \cos \omega t \quad (29)$$

such that the rate of deformation tensor is given by

$$\dot{\mathbf{\Upsilon}}(t) = \begin{bmatrix} 0 & \dot{\gamma}^0 \cos \omega t & 0 \\ \dot{\gamma}^0 \cos \omega t & 0 & 0 \\ 0 & 0 & 0 \end{bmatrix}. \quad (30)$$

Using the characteristic relaxation time of the virus suspension, λ , we can nondimensionalize Eq. (29) as

$$\lambda \dot{\gamma}(t) = \lambda \dot{\gamma}^0 \cos \lambda \omega (t/\lambda), \quad (31)$$

where $\lambda \omega$ and $\lambda \dot{\gamma}^0$ are the Deborah and Weissenberg numbers. In this paper, we focus on small-amplitude oscillatory shear flow (SAOS). For this flow field, for the molecular definition of *small amplitude*, general rigid bead–rod theory yields

$$\lambda \dot{\gamma}^0 \ll \frac{1}{v\sqrt{2}} \quad (32)$$

whose left side is the macromolecular Weissenberg number. From Eq. (32), we learn that structures with higher v will have lower limits for linear viscoelasticity.

Substituting Eqs. (10) and (29) into Eq. (21) yields the polymer contribution to the shear stress

$$\tau_p = \dot{\gamma}^0 \{ [\eta'(\omega) - \eta_s] \cos \omega t + \eta''(\omega) \sin \omega t \} \quad (33)$$

in which [Eqs. (40) and (41) of Ref. 31]

$$\frac{\eta' - \eta_s}{\eta_0 - \eta_s} = \left(\frac{1}{2b/av} + 1 \right)^{-1} \left(\frac{1}{2b/av} + \frac{1}{1 + (\lambda\omega)^2} \right), \quad (34)$$

$$\frac{\eta''}{\eta_0 - \eta_s} = \left(\frac{1}{2b/av} + 1 \right)^{-1} \frac{\lambda\omega}{1 + (\lambda\omega)^2}, \quad (35)$$

where

$$\eta^* \equiv \eta' - i\eta'' \quad (36)$$

is the complex viscosity.^{52,53} In this paper, we plot the real and imaginary parts of the responses as functions of frequency, following the work of Ferry (Secs. 2.A.4–2.A.6 of Ref. 54) or Bird *et al.* (Sec. 4.4 of Ref. 55).

As $\omega \rightarrow 0$, for the polymer contribution to the zero-shear viscosity, we get

$$\frac{\eta_0 - \eta_s}{nkT\lambda} = \frac{av}{2} + b = b \left[1 + \frac{2b}{av} \right] \left(\frac{2b}{av} \right)^{-1}, \quad (37)$$

which we use for Tables VI–IX.

Following EXAMPLE 5.2-6 of Ref. 55 and specifically by setting $n' = n = 1$ in Eq. (5.2-4) of Ref. 55, we can define a structure-dependent characteristic time,

$$\lambda_c \equiv \frac{\Psi_{0,1}}{\eta_0 - \eta_s}, \quad (38)$$

which is the ratio of the first normal stress coefficient to the viscosity at zero shear rate and thus reflects fluid elasticity. We insert Eq. (44) of Ref. 31 to get the structure-dependent characteristic time

$$\lambda_c = 2\lambda \left(\frac{1}{2b/av} + 1 \right)^{-1} \quad (39)$$

into which we insert Eq. (20) to get

$$\frac{\lambda_c}{\lambda_0} = \frac{24}{v} \left(\frac{1}{2b/av} + 1 \right)^{-1}, \quad (40)$$

which we will use below.

IV. TOBACCO MOSAIC

In this section, we test the use of general rigid bead–rod theory for predicting the complex viscosity of viruses by comparing with the measured values for tobacco mosaic virus suspensions. Although this particular virus has the form of a nanotube (see Fig. 1 of Ref. 24), since its bore is narrow, we shall approximate this rigid and rod-like virus with an osculated shish-kebab (see Table VI). From general rigid bead–rod theory we know that, for the osculated shish-kebab (TABLE XV of Ref. 31),

$$\frac{\lambda}{\lambda_0} = \frac{1}{6} N(N^2 - 1) \quad (41)$$

in which λ_0 is given by Eq. (18) and d is the diameter of the tobacco mosaic virus ($d \approx 18$ nm from Ref. 56).

We will next test Eqs. (34) and (35) against the well-known behaviors of the complex viscosities of the tobacco mosaic suspensions (see Ref. 57 and Fig. 9-3 of Ref. 54). Proceeding specifically

from the data in Fig. 14.5-1 of Ref. 22 and mindful of [Eq. (14.4-23) of Ref. 22],

$$\lambda = \frac{\eta_0 - \eta_s}{nkT} = \frac{[\eta]_0 \eta_s M}{\bar{N}kT} \quad (42)$$

so that

$$\lambda \omega = \frac{[\eta]_0 \eta_s M}{\bar{N}kT} \omega = [\eta]_0 \omega_R, \quad (43)$$

and mindful of Eqs. (4.4-16) and (4.4-17) of Ref. 55,

$$[\eta]_0 \equiv \lim_{c \rightarrow 0} \frac{\eta_0 - \eta_s}{c\eta_s}, \quad (44)$$

$$[\eta'] \equiv \lim_{c \rightarrow 0} \frac{\eta' - \eta_s}{c\eta_s}, \quad (45)$$

$$\frac{[\eta'']}{\omega} \equiv \lim_{c \rightarrow 0} \frac{\eta''/\omega}{c\eta_s} \quad (46)$$

so that for dilute virus suspensions, where

$$\frac{c}{\rho} \ll 1, \quad (47)$$

we get

$$[\eta]_0 \simeq \frac{\eta_0 - \eta_s}{c\eta_s}, \quad (48)$$

$$[\eta'] \simeq \frac{\eta' - \eta_s}{c\eta_s}, \quad (49)$$

$$\frac{[\eta'']}{\omega} \simeq \frac{\eta''/\omega}{c\eta_s} \quad (50)$$

so that

$$\frac{[\eta']}{[\eta]_0} \simeq \frac{\eta' - \eta_s}{\eta_0 - \eta_s}, \quad (51)$$

$$\frac{[\eta'']}{[\eta]_0} \simeq \frac{\eta''}{\eta_0 - \eta_s}. \quad (52)$$

We construct Fig. 6 using the best fit values of $[\eta]_0 = 23.35$ and, at $T = 310.0$ K, $\lambda = 5.20 \times 10^{-4}$ s and, at $T = 298.2$ K, $\lambda = 8.10 \times 10^{-4}$ s. By Eq. (22), these correspond to rotational diffusivities at $T = 310.0$ K and $D_r = 321$ s $^{-1}$ and at $T = 298.2$ K and $D_r = 206$ s $^{-1}$.

In passing, mindful of the caption of Fig. 14.5-1 of Ref. 22, we calculate the dimensional relaxation times for the tobacco mosaic virus suspensions in Fig. 6 at $T = 310.0$ K,

$$\begin{aligned} \lambda &= \frac{[\eta]_0 \eta_s M}{\bar{N}kT} \\ &= \frac{20(\text{cm}^3/\text{g})3.43 \times 10^{-3}(\text{Pa s})3.9 \times 10^7(\text{g/mol})}{6.022 \times 10^{23}(\text{mol}^{-1})1.380 \times 10^{-23}(\text{J/K})310.0(\text{K})} \\ &= 1.04 \times 10^{-3} \text{ s}, \end{aligned} \quad (53)$$

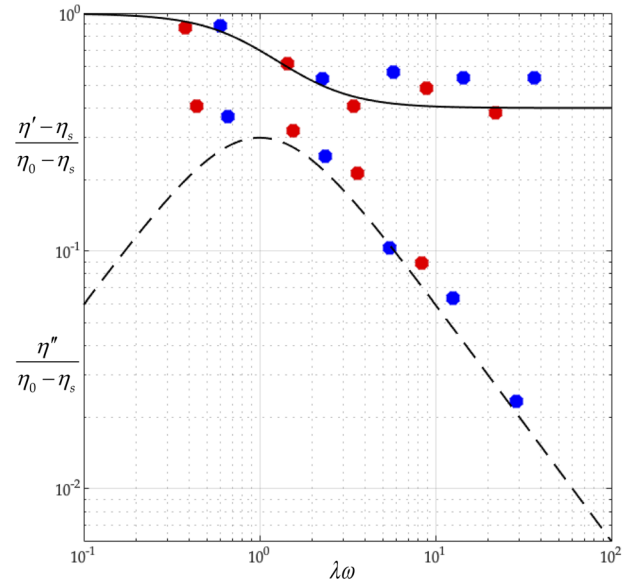


FIG. 6. The dimensionless complex viscosity of tobacco mosaic virus suspension predicted by the general rigid bead-rod theory vs experimental data (Fig. 14.5-1 of Ref. 22). The data are for solutions of tobacco mosaic virus of $M = 3.9 \times 10^7$ g/mol. The red points represent data taken at 310 K, and the blue ones are taken at 298.2 K. The solvent viscosity at the two temperatures is $\eta_s = 3.43 \times 10^{-3}$ Pa s and $\eta_s = 5.16 \times 10^{-3}$ Pa s, respectively. The general rigid bead-rod theory predictions are computed using a value $[\eta]_0 = 18$ cm 3 /g as the best fit with the data. The solid curve describes $(\eta' - \eta_s)/(\eta_0 - \eta_s)$, and the dashed one describes $\eta''/(\eta_0 - \eta_s)$.

and at $T = 298.2$ K,

$$\begin{aligned} \lambda &= \frac{[\eta]_0 \eta_s M}{\bar{N}kT} \\ &= \frac{20(\text{cm}^3/\text{g})5.16 \times 10^{-3}(\text{Pa s})3.9 \times 10^7(\text{g/mol})}{6.022 \times 10^{23}(\text{mol}^{-1})1.380 \times 10^{-23}(\text{J/K})298.2(\text{K})} \\ &= 1.62 \times 10^{-3} \text{ s}. \end{aligned} \quad (54)$$

The fitted value $[\eta]_0 = 23.35$ falls below the reported theoretical value of $[\eta]_0 = 27$ (see the caption of Fig. 14.5-1 of Ref. 22).

Solving Eq. (52) for the integer number of beads in the oscillated shish-kebab,

$$N = \frac{(\sqrt{243\Lambda^2 - 1} + \Lambda\sqrt{3^5})^{2/3} + 1}{\sqrt{3}(\sqrt{243\Lambda^2 - 1} + \Lambda\sqrt{3^5})^{1/3}}, \quad (55)$$

where

$$\Lambda \equiv \frac{\lambda}{\lambda_0} \quad (56)$$

and where the right side of Eq. (55) is rounded to the nearest integer. Using Eq. (18) and for $d \simeq 18$ nm, at $T = 310.0$ K, we get

$$\lambda_0 = \frac{\pi}{4} \frac{(18 \times 10^{-9})^3 3.43 \times 10^{-3}(\text{Pa s})}{1.380 \times 10^{-23}(\text{J/K})310.0(\text{K})} = 3.67 \times 10^{-6} \text{ s}, \quad (57)$$

and at $T = 298.2$ K,

$$\lambda_0 = \frac{\pi (18 \times 10^{-9})^3 5.16 \times 10^{-3} (\text{Pa s})}{4 \cdot 1.380 \times 10^{-23} (\text{J/K}) 298.2 (\text{K})} = 5.74 \times 10^{-6} \text{ s}. \quad (58)$$

Thus, using Eq. (57) with the fitted value of $\lambda = 5.20 \times 10^{-4}$ s for $T = 310.0$ K gives $\Lambda = 283$, and so, Eq. (55) gives $N = 12$. Similarly, using that with $\lambda = 8.10 \times 10^{-4}$ s for $T = 298.2$ K gives $\Lambda = 282$, and so, $N = 12$. From this, we learn that the tobacco mosaic virus can be modeled with an osculated shish-kebab of 12 beads, for which Table III lists the position vectors (see Fig. 1).

Recall that, below Eq. (52), we found that at $T = 310.0$ K, $D_r = 321 \text{ s}^{-1}$ (or $\lambda_0 D_r = 1.17 \times 10^{-3}$), and at $T = 298.2$ K, $D_r = 206 \text{ s}^{-1}$ (or $\lambda_0 D_r = 1.18 \times 10^{-3}$). These values compare closely with the value predicted by Eq. (23) for an osculated shish-kebab of $N = 12$. Furthermore, from the available measurements (all non-rheological), the rotational diffusivity range for the tobacco mosaic virus at room temperature (20°C – 25°C) is^{38–43}

$$285 \leq D_r \leq 400 \text{ s}^{-1}. \quad (59)$$

Our value of $D_r = 206 \text{ s}^{-1}$, fitted to complex viscosity measurements (Fig. 6), falls just below this range.

In this section, we have approximated this rigid and rod-like virus with an osculated shish-kebab. However, its detailed structure of a narrow-bore nanotube consisting of the osculated helix of beads shown in Fig. 1. of Ref. 24 can be captured using Eqs. (5) and (6) of Ref. 28, where $L = d$. We leave this for another day.

V. GEMINI

In this section, we use general rigid bead-rod theory to model the gemini virus as twin truncated icosahedra. To illustrate these

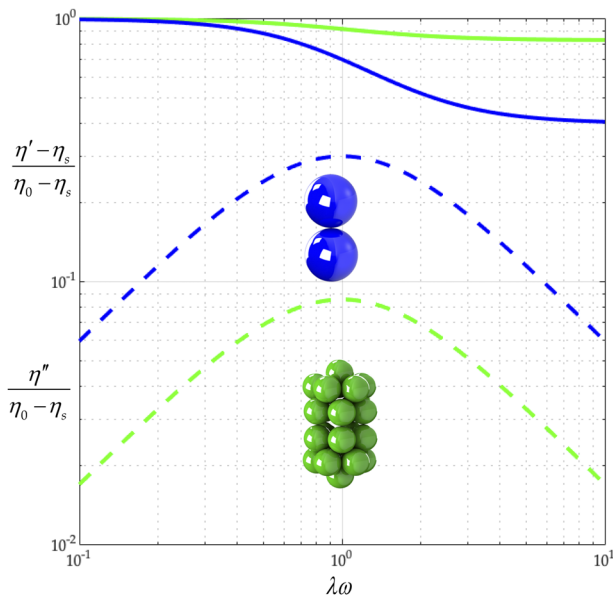


FIG. 7. Gemini virus complex viscosity comparison: two osculating beads (green) and twin icosahedra (blue). The solid curve describes $(\eta' - \eta_s)/(\eta_0 - \eta_s)$, and the dashed one describes $\eta''/(\eta_0 - \eta_s)$.

twin truncated icosahedra, we construct Fig. 2 from the position vectors in Table III. We then compare this twin icosahedral structure to its coarser simpler cousin, two osculating beads ($L = 2R$). From Table VII, we learn that the finer twin icosahedral structure of the gemini virus increases both λ/λ_0 and $(\eta_0 - \eta_s)/nkT\lambda$ over two osculating beads. From this, we deepen our understanding of the role played by the finer twin truncated icosahedral structure.

By comparing the values of $\lambda_0 D_r$ in Table VII, we discover that a twin icosahedral gemini model gives a lower rotational diffusivity than for twin osculating beads. Using the values of $2b/av$ for the gemini virus in Table VII, with Eqs. (34) and (35), we construct Fig. 7 from which we first learn that for twin truncated icosahedra, $(\eta' - \eta_s)/(\eta_0 - \eta_s)$ descends less sharply than for twin osculating beads. We also learn that for the twin truncated icosahedral structure, $\eta''/(\eta_0 - \eta_s)$ falls below that of the twin osculating beads. We thus find that the fine structure of the gemini virus matters, raising viscosity and lowering elasticity.

VI. ADENOVIRUS

To arrive at the rotational diffusivity of the adenovirus, we follow the method of Sec. II. The adenovirus capsid (not including peplomers) is made up of 252 capsomers in an icosahedral arrangement (plate II of Ref. 58). Twelve of these are “pentons” with five nearest neighbors, and the other 240 are “hexons” with six nearest neighbors.

An icosahedron has 20 triangular faces, 30 edges, and 12 vertices. Each vertex holds a penton, shared by five edges and five faces. The faces are made of two nested triangular arrangements, the inner triangle being made of six hexons. Each of 120 edge hexons is shared by two faces. Each of the 120 face hexons belongs to a single face, with all six of its neighbors lying in that face.

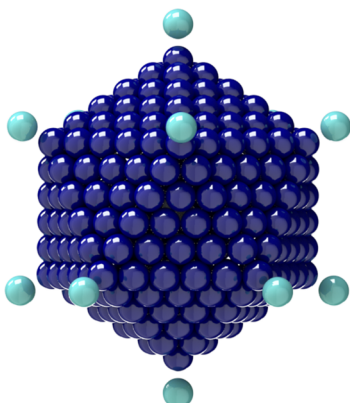
The edges are taken to have length $5L$, with the interparticle distance L equal to the diameter d of the capsomer. The 12 vertices sit on the edges of three rectangles with Cartesian coordinates given by cyclic permutations of $(\pm\beta, \pm 1, 0)$ scaled by $5L/2$, where $\beta = (1 + \sqrt{5})/2$ is the golden ratio. This exploits the fact that $\sqrt{1 + \beta^2 + (\beta - 1)^2} = 2$. We designate the position vectors \mathbf{V}_i of the 12 vertices in Table IV. The edge vectors are thus $\mathbf{E}_{ij} = \mathbf{V}_j - \mathbf{V}_i$, where, for example, $\mathbf{E}_{0111} = \mathbf{V}_{11} - \mathbf{V}_{01}$.

To describe face beads, we need twelve sets of five triplets ijk arising from a counterclockwise enumeration of the five neighboring vertices associated with one vertex. We encode this as follows: The notation 01: 02, 11, 06, 05, 09 means faces $ijk = 010\ 211, 011\ 106, 010\ 605, 010\ 509, 010\ 902$. Table V lists our twelve sets.

We associate two edge beads on five edges and two face beads (this is a chiral choice) on five faces with each vertex, so that each of the 12 vertices \mathbf{V}_i with $i = 1, 2, \dots, 12$ is associated with five triplets ijk and the following 21 points: the vertex itself, \mathbf{V}_i , to which we add vectors for the ten edge beads, $\frac{1}{5}\mathbf{E}_{ij}$ and $\frac{2}{5}\mathbf{E}_{ij}$, and ten face beads, $\frac{1}{5}(\mathbf{E}_{ij} + \mathbf{E}_{ik})$ and $\frac{1}{5}(2\mathbf{E}_{ij} + \mathbf{E}_{ik})$. Following this method, we arrive at the position vectors \mathbf{R}_i of the adenovirus capsid beads so that $i = 1, 2, \dots, 252$.

Oliver, who measured the translational diffusivity of the adenovirus,³⁷ overlooked the identity [Eq. (28)] when he wrote “the rotational diffusivity of the adenovirus appears to be zero.” Perhaps

TABLE IV. Twelve vertices of the adenovirus capsid.

Macromolecule	\mathbf{V}_i
	$\mathbf{V}_{01} = \frac{5L}{2}(\beta, 1, 0), \mathbf{V}_{02} = \frac{5L}{2}(\beta, -1, 0)$
	$\mathbf{V}_{03} = \frac{5L}{2}(-\beta, 1, 0), \mathbf{V}_{04} = \frac{5L}{2}(-\beta, -1, 0)$
	$\mathbf{V}_{05} = \frac{5L}{2}(0, \beta, 1), \mathbf{V}_{06} = \frac{5L}{2}(0, \beta, -1)$
	$\mathbf{V}_{07} = \frac{5L}{2}(0, -\beta, 1), \mathbf{V}_{08} = \frac{5L}{2}(0, -\beta, -1)$
	$\mathbf{V}_{09} = \frac{5L}{2}(1, 0, \beta), \mathbf{V}_{10} = \frac{5L}{2}(-1, 0, \beta)$
	$\mathbf{V}_{11} = \frac{5L}{2}(1, 0, -\beta), \mathbf{V}_{12} = \frac{5L}{2}(-1, 0, -\beta)$

this explains why the transport property, rotational diffusivity, has been largely overlooked in virology.

From general rigid bead-rod theory [Eq. (23)], for the characteristic time of the adenovirus, we get

$$\lambda_0 \equiv \frac{\nu}{72D_r}, \tag{60}$$

and then, inserting Eq. (26) gives

$$\lambda_0 \equiv \frac{L^2}{6D_{rot}} \tag{61}$$

into which we insert the identity Eq. (27) to get

$$\frac{\lambda_0}{L^2} \equiv \frac{1}{24D_{tr}} \tag{62}$$

into which we next insert Eq. (16),

$$\frac{\lambda_0}{L^2} = \frac{\zeta}{12kT} = \frac{\pi d \eta_s}{4kT} = \frac{1}{24D_{tr}}. \tag{63}$$

TABLE V. Twelve sets of five triplets describing the faces of the adenovirus capsid.

Vertex i	Neighboring vertices jk
01	02, 11, 06, 05, 09
02	11, 01, 09, 07, 08
03	04, 10, 05, 06, 12
04	03, 12, 08, 07, 10
05	06, 03, 10, 09, 01
06	05, 01, 11, 12, 03
07	08, 02, 09, 10, 04
08	07, 04, 12, 11, 02
09	10, 07, 02, 01, 05
10	09, 05, 03, 04, 07
11	12, 06, 01, 02, 08
12	11, 08, 04, 03, 06

Now, from Ref. 37, we have the measured value of the translational diffusivity for the adenovirus at body temperature,

$$D_{tr} \simeq 0.367 \times 10^{-7} \text{ cm}^2/\text{s}. \tag{64}$$

Substituting this into Eq. (63),

$$\frac{\lambda_0}{L^2} = \frac{1}{24(0.367 \times 10^{-7} \text{ cm}^2/\text{s})} = 1.14 \times 10^6 \text{ s/cm}^2, \tag{65}$$

which establishes the correspondence between our general rigid bead-rod model of the adenovirus (see in Table VIII) and the adenovirus particle itself.

From the available microscopy (see Fig. 11 of Ref. 59), $r_c \simeq 116 \text{ nm}$ (between opposing vertices), and the range for the virus radius, made dimensionless with the capsid radius, is given by

$$\frac{6}{5} \leq \frac{r_v}{r_c} \leq \frac{4}{3}. \tag{66}$$

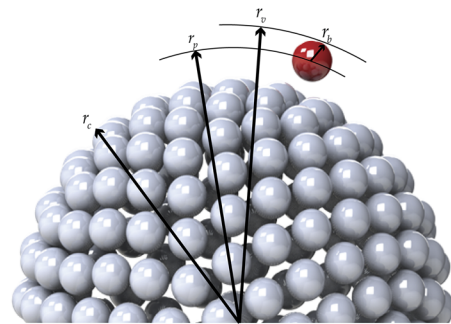


FIG. 8. Connections between coronavirus particle dimensions and its general rigid bead-rod model. For the peplomer bulb, we have bead radius $r_b \equiv \frac{1}{2}d$ so that for the peplomer height, we have $r_v - r_c = r_p + r_b = r_p + \frac{1}{2}d$ (see Table X). The peplomer head radial position is thus the center to center distance between the peplomer head and the capsid ($r_v - r_b$).

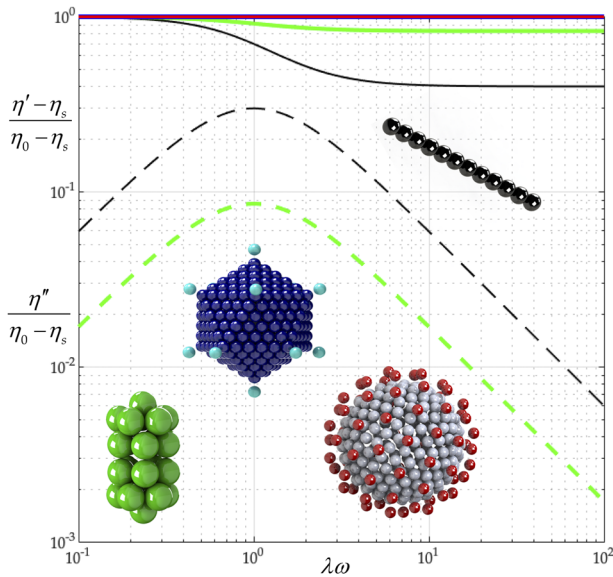


FIG. 9. Tobacco mosaic (black), gemini (green), adeno (blue), and corona (red) complex viscosity comparison. The solid curve describes $(\eta' - \eta_s)/(\eta_0 - \eta_s)$, and the dashed one describes $\eta''/(\eta_0 - \eta_s)$.

We thus position one bead for each adenovirus spike along each of the 12 vertices using $r_v/r_c = 5/4$ (see Fig. 3), which satisfies Eq. (66). Using $r_c \approx 116$ nm and mindful of the adenovirus geometry (see Fig. 3) and its dimensions (see Fig. 4), we get $L = 12.4$ nm. Inserting this into Eq. (65) gives

$$\lambda_0 = 1.75 \times 10^{-6} \text{ s}, \tag{67}$$

namely, the characteristic time, from general rigid bead-rod theory, for the adenovirus.

VII. CORONAVIRUS

The coronavirus particle is a biological material whose dimensions are thus known to within biological experimental error. From the available microscopy, $r_c \approx 100$ nm–133 nm,⁶⁰ and thus, the range for the virus radius, made dimensionless with the capsid radius, is

given by (see Table X and Fig. 8)

$$\frac{5}{4} \leq \frac{r_v}{r_c} \leq \frac{4}{3}. \tag{68}$$

Each trimeric peplomer head, consisting of three glycoproteins, is equilateral triangular when viewed along the spike axis (see Fig. 14). For the purposes of the general rigid bead-rod theory, we must replace this trimer with a sphere of radius r_b . For this sphere, we choose a diameter, $2r_b$, matching the length of the equilateral triangle (compare Fig. 8 with Fig. 14). From the available published SARS-CoV spike structure, $r_b \approx 6.5$ nm and the peplomer height $r_v - r_c \approx 13.0$ nm.⁶¹ From this, we learn that the SARS-CoV spike is equidimensional, that is, $2r_b/(r_v - r_c) \approx 1$. In general rigid bead-rod theory, we approximate the bulbous SARS-CoV-2 triglycoprotein head with a single bead so that $2r_b = d$. From the available microscopy, we can see that the range for the triglycoprotein head diameter, made dimensionless with the capsid diameter, is given by (see Table X and Fig. 8)

$$\frac{35}{2} \leq \frac{r_c}{r_b} \leq \frac{41}{2}. \tag{69}$$

When viewed through the lens of general rigid bead-rod theory, we learn that the rotational diffusivity of the coronavirus and its associated rheological properties are conferred by the particle shape and not by the ratio r_c/r_b .

General rigid bead-rod theory requires the particle to be modeled with beads of the same size. For the coronavirus, we match this bead size, r_b , to the finest relevant part of the coronavirus structure: the peplomer head (see Fig. 8). The much larger capsid must therefore be beaded, with beads of radii r_b .

In this work, we choose the measured peplomer population $N_p = 74$ (Table X) over the postulated value $N_p = 90$ (Table X). To construct the specific coronavirus example of Fig. 5 ($N_c = 256$, $N_p = 74$, and $r_v/r_c = 5/4$), we begin by beading a unit sphere for the capsid around which we arrange a constellation of peplomer heads. We get position vectors for these beads by multiplying the 74 point-charge solution to the Thomson problem extracted from Ref. 29 of Ref. 25 by 5/4.

Since the trimeric peplomer heads are charged identically, we expect the spikes to arrange themselves following the polyhedral solutions to the Thomson problem.^{25,26} We learn that these polyhedral solutions are all at least nearly axisymmetric,³¹ but few are exactly so. By *nearly axisymmetric*, we mean that the moments of inertia about the transverse molecular axes, I_1 and I_2 , hardly differ. In other words, *nearly axisymmetric* means that the average value of the moments of inertia about the transverse molecular axes,

TABLE VI. Tobacco mosaic characteristics from general rigid bead-rod theory.


Macromolecule	$\frac{I_1}{mL^2}, \frac{I_2}{mL^2}$	$\frac{I_3}{mL^2}$	a	b	ν	$\frac{2b}{av}$	$\frac{\eta_0 - \eta_s}{nkT\lambda}$	$\frac{\lambda}{\lambda_0}$	$\lambda_0 D_r$	$\frac{\Psi_{0,1}}{\lambda(\eta_0 - \eta_s)}$
	143	0	$\frac{286}{15}$	$\frac{3}{5}$	$\frac{6}{143}$	$\frac{3}{2}$	1	286	$\frac{1}{1716}$	$\frac{6}{5}$

TABLE VII. Gemini characteristics from general rigid bead–rod theory: Twin icosahedra vs two osculating beads models.


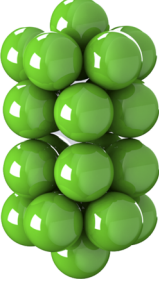
Macromolecule	$\frac{I_1}{mL^2}, \frac{I_2}{mL^2}$	$\frac{I_3}{mL^2}$	a	b	ν	$\frac{2b}{av}$	$\frac{\eta_0 - \eta_s}{nkT\lambda}$	$\frac{\lambda}{\lambda_0}$	$\lambda_0 D_r$	$\frac{\Psi_{0,1}}{\lambda(\eta_0 - \eta_s)}$
	$\frac{1}{2}$	0	$\frac{1}{15}$	$\frac{3}{5}$	12	$\frac{3}{2}$	1	1	$\frac{1}{6}$	$\frac{6}{5}$
	35.02	14.47	11.67	0.2065	0.1713	0.2065	1.207	70.04	0.002 379	0.3423

TABLE VIII. Adenovirus characteristics from general rigid bead–rod theory.

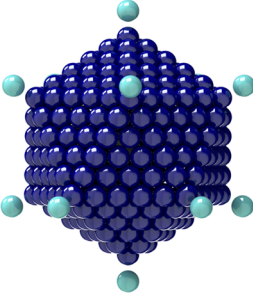
Macromolecule	$\frac{I_1}{mL^2}, \frac{I_2}{mL^2}$	$\frac{I_3}{mL^2}$	a	b	ν	$\frac{2b}{av}$	$\frac{\eta_0 - \eta_s}{nkT\lambda}$	$\frac{\lambda}{\lambda_0}$	$\lambda_0 D_r$	$\frac{\Psi_{0,1}}{\lambda(\eta_0 - \eta_s)}$
	3082	3082	1541	0	0.001 947	0	$\frac{3}{2}$	6163	0.000 027 04	0

TABLE IX. Coronavirus characteristics for different capsid beadings from general rigid bead–rod theory.

SARS-CoV-2	$\frac{I_1}{mL^2}$	$\frac{I_2}{mL^2}$	$\frac{I_3}{mL^2}$	a	b	ν	$\frac{2b}{av}$	$\frac{\eta_0 - \eta_s}{nkT\lambda}$	$\frac{\lambda}{\lambda_0}$	$\lambda_0 D_r$	$\frac{\Psi_{0,1}}{\lambda(\eta_0 - \eta_s)}$
$N_c = 16, N_p = 74$	87.76	87.71	87.79	43.88	9.52×10^{-8}	6.84×10^{-2}	6.34×10^{-8}	1.50	175.51	9.50×10^{-4}	1.27×10^{-7}
$N_c = 32, N_p = 74$	98.42	98.37	98.46	49.22	7.57×10^{-8}	6.10×10^{-2}	5.04×10^{-8}	1.50	196.85	8.47×10^{-4}	1.01×10^{-7}
$N_c = 64, N_p = 74$	143.77	143.66	143.80	71.90	1.86×10^{-8}	4.17×10^{-2}	1.24×10^{-8}	1.50	287.55	5.80×10^{-4}	2.48×10^{-8}
$N_c = 128, N_p = 74$	162.41	162.40	162.45	81.21	3.28×10^{-8}	3.69×10^{-2}	2.18×10^{-8}	1.50	324.82	5.13×10^{-4}	4.36×10^{-8}
$N_c = 256, N_p = 74$	247.76	247.70	247.79	123.88	1.19×10^{-8}	2.24×10^{-2}	7.96×10^{-9}	1.50	495.51	3.36×10^{-4}	1.60×10^{-8}
$N_c = 510, N_p = 74$	417.10	417.02	417.12	208.56	7.50×10^{-10}	1.44×10^{-2}	4.50×10^{-10}	1.50	834.21	2.00×10^{-4}	9.0×10^{-10}

$\frac{1}{2}(I_1 + I_2)$, hardly differs from I_1 . In dimensionless terms, nearly axisymmetric thus means

$$\left| \frac{I_2 - I_1}{2I_1} \right| \ll 1 \tag{70}$$

to which Eqs. (34) and (35) are subject. For the reported polyhedral solutions to the Thomson problem,^{25,26}

$$\left| \frac{I_2 - I_1}{2I_1} \right| = o(10^{-4}), \tag{71}$$

which satisfies Eq. (70). The method of this section can be used for any spiked virus with a spherical capsid, including the insect Pariacoto virus [Fig. 22(a) of Ref. 62].

Figure 9 combines results on all four of our viruses (from Sec. IV to the present section) using the calculated $2b/av$ values from Tables VI–IX (row 6 of Table IX). From Fig. 9, we learn that $(\eta' - \eta_s)/(\eta_0 - \eta_s)$ curves for the adeno- and coronavirus bead-rod models descend less sharply than those of tobacco mosaic or gemini viruses. From Fig. 10, we learn that the higher the complexity (coronavirus), the lower the $\eta''/(\eta_0 - \eta_s)$, and thus, the lower the dimensionless elasticity. We also learn that adenovirus is *spherically symmetrical* ($I_1 = I_2 = I_3$), and thus, it is not associated with $\eta''/(\eta_0 - \eta_s)$.

A. Capsid beading

In this subsection, we vary the capsid beading of the coronavirus particle, N_c , and fix the peplomer bead number, $N_p = 74$. We model the different capsid beadings, $N_c = 16, 32, 64, 128, 256, 510$, and thus construct Table IX. By comparing the values of λ/λ_0 in Table IX, we learn that making the capsid beading finer (increasing N_c) increases the relaxation time. By examining the values of

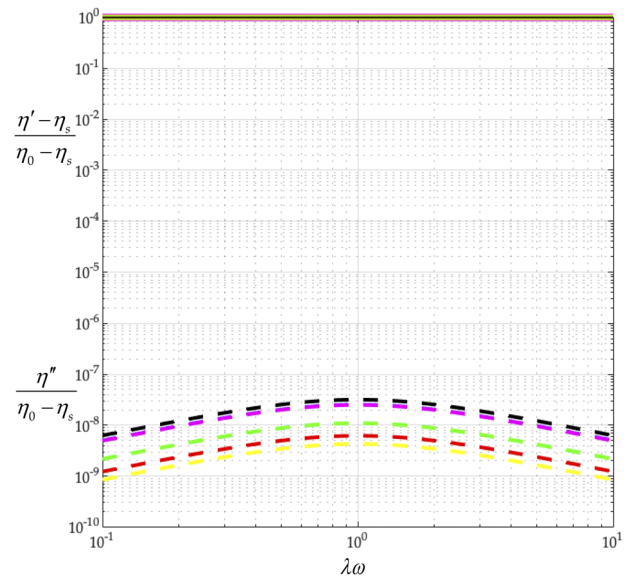


FIG. 11. Effect of capsid osculated beadings on complex viscosity ($N_c = 16, 32, 64, 128, 256, 510, N_p = 74, r_v/r_c = 5/4$, and $L = d$). $N_c = 16$ (black), $N_c = 32$ (blue), $N_c = 64$ (red), $N_c = 128$ (green), $N_c = 256$ (yellow), and $N_c = 510$ (magenta). The solid curve describes $(\eta' - \eta_s)/(\eta_0 - \eta_s)$, and the dashed one describes $\eta''/(\eta_0 - \eta_s)$.

$(\eta_0 - \eta_s)/nkT\lambda$ in Table IX, we also learn that increasing N_c does not affect the polymer contribution to zero-shear viscosity, since $(\eta_0 - \eta_s)/nkT\lambda$ remains 1.5. From Table IX, we learn that dimensionless rotational diffusivity, $\lambda_0 D_r$, decreases with N_c .

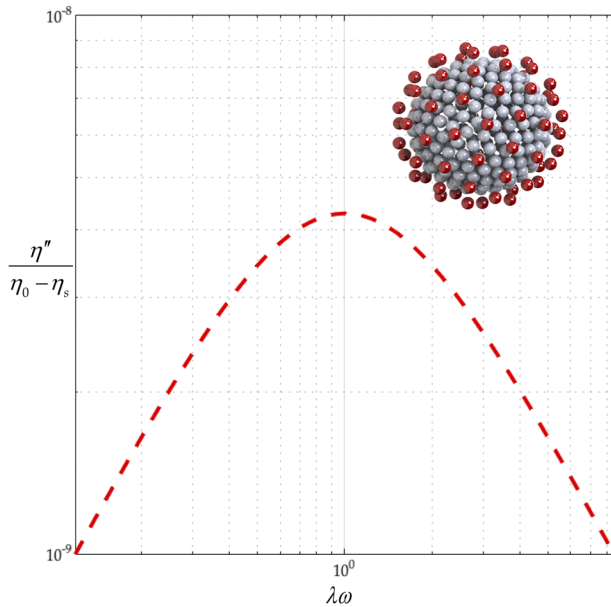


FIG. 10. Corona (red) elastic complex viscosity, $\eta''/(\eta_0 - \eta_s)$, curve.

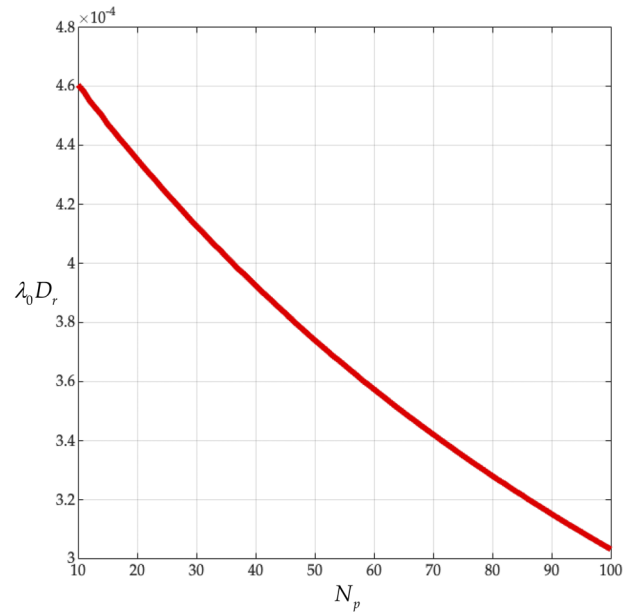


FIG. 12. Dimensionless rotational diffusivity $\lambda_0 D_r$ from Eq. (23) vs peplomer population N_p ($N_c = 256$).

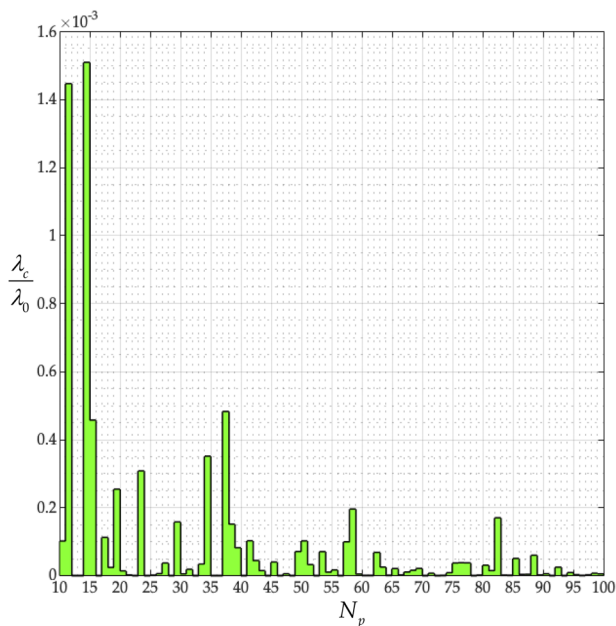


FIG. 13. Dimensionless structure-dependent characteristic time, λ_c/λ_0 , vs peplomer population, N_p ($N_c = 256$), from Eq. (40).

Using the values of $2b/av$ for all coronavirus capsid beadings in Table VII, with Eqs. (34) and (35), we construct Fig. 11 from which we first learn that increasing N_c does not change $(\eta' - \eta_s)/(\eta_0 - \eta_s)$. A coronavirus model thus always gives a nearly constant viscosity (nearly spherically symmetric).

B. Peplomer population

In this subsection, we fix the capsid beading of the coronavirus particle at $N_c = 256$ and vary the peplomer bead population over $10 \leq N_p \leq 100$ to get Figs. 12 and 13. From Fig. 12, we learn that rotational diffusivities of the coronavirus, made dimensionless with the constant λ_0 , are of order 10^{-4} . Specifically, for the measured peplomer population, $N_p = 74$ (see Table X), we get $\lambda_0 D_r = 3.36 \times 10^{-4}$. This value exceeds the dimensionless diffusivity of the adenovirus (Table VIII) and falls below those of the tobacco mosaic (Table VI) and gemini viruses (Table VII). The binding interval for the SARS-CoV-2 particle exceeds 3 min [see Fig. 3(A) of Ref. 1 and Refs. 61 and

63], and thus, it would appear that coronavirus peplomer binding prefers $\lambda_0 D_r = o(10^{-4})$.

Equation (39) defines a structure-dependent characteristic time, λ_c , and the ratio of the first normal stress coefficient to the viscosity at zero shear rate. Specifically, we next explore how λ_c depends on the peplomer population. Nondimensionalizing λ_c with the constant λ_0 , produces the staircase plot of Fig. 13, which is not monotonic. From Fig. 13, we learn that the characteristic times of the coronavirus particles, made dimensionless with the λ_0 , over $10 \leq N_p \leq 100$, fall below 10^{-4} . In other words, the elasticity of the coronavirus particles is slight and is not monotonic with N_p . Furthermore, at the measured peplomer population of $N_p = 74$ (Table X), λ_c/λ_0 is vanishingly small.

In this subsection, we have explored the role of N_p on the transport properties of the coronavirus particle and found that its precise value matters. Such precise values for N_p , be it for SARS-CoV-2, SARS-CoV, or any other spiked virus with a spherical capsid, have yet to be reported.

VIII. CONCLUSION

We find that our *ab initio* calculations agree with the observed complex viscosity of the tobacco mosaic virus suspension (Fig. 6). From our analysis of the gemini virus suspension, we learn that the fine detail of the virus structure governs its rotational diffusivity (Fig. 7). We find that combining our *ab initio* calculations with the observed rotational diffusivity of the adeno suspension yields the characteristic time, from general rigid bead-rod theory, for the adenovirus (Sec. VI). Finally, from our analysis of the coronavirus suspension (Sec. VII), we learn that its rotational diffusivity descends monotonically with its peplomer population (Fig. 12).

In Sec. VII, we tackled spiked viruses with spherical capsids for which $b \approx 0$. However, histologically, SARS-CoV-2 capsids present with pleomorphism (Fig. 3 of Ref. 64). We leave the rotational diffusivity of spiked viruses of non-spherical (including ellipsoidal) capsids, for which $b > 0$, for another day.

In Sec. IV, we learned how to deduce the rotational diffusivity of a virus by fitting the measured values of the real and imaginary parts of the complex viscosity function to the main results from general rigid bead-rod theory [Eqs. (34) and (35)]. However, complex viscosity measurements on SARS-CoV-2 suspensions are unavailable, and their measurement is understandably dangerous. Perhaps

TABLE X. Physical dimensions of coronaviruses (see Fig. 8). $p \equiv$ postulated.

Macromolecule	r_c (nm)	r_v (nm)	$\frac{r_v}{r_c}$	$r_v - r_c$ (nm)	r_b (nm)	N_p	References
SARS-CoV-2		30–70		9–12			64
SARS-CoV		39					68
SARS-CoV		44–47					Section 3 of Ref. 60
SARS-CoV						74, 90 ^p	Section 4.1 of Ref. 60
SARS-CoV	100–133		1.25–1.53				Figure 1(D) of Ref. 60
SARS-CoV				13.0	6.5		6CRZ.PDB from Ref. 61

the method of microrheology, which requires just one drop of SARS-CoV-2 suspension, will yield its complex viscosity measurements (see Refs. 65 and 66 and Chaps. 4 and 5 of Ref. 67).

If the dimer target is projected onto the peplomer orientation distribution function, the integral (in phase space) under this projection gives the probability of one spike aligning properly for fusion, p . Since, for fusion, we need two adjacent spikes to align, the probability falls well below p . Equations (1) and (2) consider just one special case of alignment. We leave the integral (in phase space) over all possible alignments for another day.

Our macromolecular bead-rod model viruses are suspended in a Newtonian solvent. We neglect interactions of the solvent velocity fields, be they between nearest beads (see Refs. 48 and 49 and Sec. 14.6 of Ref. 22) or nearest macromolecules. We leave the effects of these hydrodynamic interactions on rotational diffusivity for another day.

Whereas the bulbous head of a peplomer is trimeric and therefore triangular, in this work, we have represented the bulb with a single bead. Figure 14 illustrates this model. We thus propose incorporating the triangularity of the bulbous peplomer by replacing its head with three identically charged osculating beads. The potential energy minimization for these three-beaded bulbs will, of course, produce new and interesting polyhedra differing from the Thomson solutions used herein.^{25,26} We leave this potential energy minimization, polyhedra discovery, and corresponding *ab initio* rotational diffusivity calculation for another day.

Under the microscope, we see some agglomeration of coronavirus particles, mechanically interlocked by interdigitation of the bulbous spikes [see Fig. 1(D) of Ref. 60]. The simplest of these agglomerates is a pair. We leave the calculation of the diffusivity of such interdigitated coronavirus structures from general rigid bead-rod theory for another day.

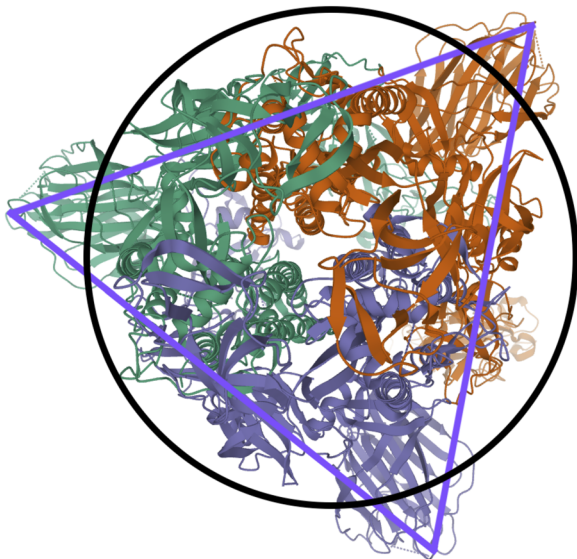


FIG. 14. In this work, we replace the peplomer bulk with sphere (a) inscribed in the trimer, thus neglecting its triangularity. Future work shall improve upon this by inscribing the trimer (b) into three osculating beads.⁶¹

For this work, for both adenovirus and coronavirus, we chose the ratio $r_o/r_c = 5/4$ (Figs. 3 and 5, respectively), which is consistent with the available microscopy [Eqs. (66) and (68), respectively]. We leave the exploration of the rotational diffusivities over these dimensionless spike length ranges for another day.

Whereas in engineering, the complex viscosity function has a broad diversity of applications including polymer or suspension processing, for virus suspensions, its main use is for determining rotational diffusivity. The uninitiated might expect that our complex viscosity equations for the adenovirus [Eqs. (34) and (35) with Table VIII] or coronavirus [Eqs. (34) and (35) with Table IX] suspensions might be useful for cough or sneeze cloud modeling. However, such cloud droplets are not merely virus particle suspensions but suspend the materials that virus infected lungs or nasal passages produce.

More broadly, our vision here is that a handbook of general rigid bead-rod virus models be generated eventually from which the transport properties of any included virus might be calculated and then compared. Such a handbook might thus lead us to deepen our understanding of the relation between the rotational diffusivities of virus particles and their intricate shapes.

ACKNOWLEDGMENTS

This research was undertaken, in part, thanks to support from the Canada Research Chairs program of the Government of Canada for the Natural Sciences and Engineering Research Council of Canada (NSERC) Tier 1 Canada Research Chair in Rheology. This research was also undertaken, in part, thanks to support from the Discovery Grant program of the Natural Sciences and Engineering Research Council of Canada (NSERC) (A. J. Giacomini), the Vanier Canada Graduate Scholarship (M. A. Kalso), and the Mitacs Research Training Award (A. J. Giacomini and M. A. Kalso). A. J. Giacomini is indebted to the Faculty of Applied Science and Engineering of Queen's University at Kingston for its support through a Research Initiation Grant (RIG). We acknowledge the help of Professor Khemapat Tontiwattanakul of King Mongkut's University of Technology North Bangkok with our solid modeling computer-aided design.

DATA AVAILABILITY

The data that support the findings of this study are available within the article.

REFERENCES

- ¹D. Wrapp, N. Wang, K. S. Corbett, J. A. Goldsmith, C.-L. Hsieh, O. Abiona, B. S. Graham, and J. S. McLellan, "Cryo-EM structure of the 2019-nCoV spike in the prefusion conformation," *Science* **367**(6483), 1260–1263 (2020).
- ²R. Yan, Y. Zhang, Y. Li, L. Xia, Y. Guo, and Q. Zhou, "Structural basis for the recognition of SARS-CoV-2 by full-length human ACE2," *Science* **367**(6485), 1444–1448 (2020).
- ³T. Dbouk and D. Drikakis, "On coughing and airborne droplet transmission to humans," *Phys. Fluids* **32**(5), 053310 (2020).
- ⁴R. Bhardwaj and A. Agrawal, "Likelihood of survival of coronavirus in a respiratory droplet deposited on a solid surface," *Phys. Fluids* **32**(6), 061704 (2020).
- ⁵S. Verma, M. Dhanak, and J. Frankenfield, "Visualizing the effectiveness of face masks in obstructing respiratory jets," *Phys. Fluids* **32**(6), 061708 (2020).

- ⁶T. Dbouk and D. Drikakis, "On respiratory droplets and face masks," *Phys. Fluids* **32**(6), 063303 (2020).
- ⁷S. Chaudhuri, S. Basu, P. Kabi, V. R. Unni, and A. Saha, "Modeling the role of respiratory droplets in COVID-19 type pandemics," *Phys. Fluids* **32**(6), 063309 (2020).
- ⁸Y.-Y. Li, J.-X. Wang, and X. Chen, "Can a toilet promote virus transmission? From a fluid dynamics perspective," *Phys. Fluids* **32**(6), 065107 (2020).
- ⁹G. Busco, S. R. Yang, J. Seo, and Y. A. Hassan, "Sneezing and asymptomatic virus transmission," *Phys. Fluids* **32**(7), 073309 (2020).
- ¹⁰R. Bhardwaj and A. Agrawal, "Tailoring surface wettability to reduce chances of infection of COVID-19 by a respiratory droplet and to improve the effectiveness of personal protection equipment," *Phys. Fluids* **32**(8), 081702 (2020).
- ¹¹J.-X. Wang, Y.-Y. Li, X.-D. Liu, and X. Cao, "Virus transmission from urinals," *Phys. Fluids* **32**(8), 081703 (2020).
- ¹²P. Prasanna Simha and P. S. Mohan Rao, "Universal trends in human cough airflows at large distances," *Phys. Fluids* **32**(8), 081905 (2020).
- ¹³J. Plog, J. Wu, Y. J. Dias, F. Mashayek, L. F. Cooper, and A. L. Yarin, "Reopening dentistry after COVID-19: Complete suppression of aerosolization in dental procedures by viscoelastic Medusa Gorgo," *Phys. Fluids* **32**(8), 083111 (2020).
- ¹⁴C. P. Cummins, O. J. Ajayi, F. V. Mehendale, R. Gabl, and I. M. Viola, "The dispersion of spherical droplets in source-sink flows and their relevance to the COVID-19 pandemic," *Phys. Fluids* **32**(8), 083302 (2020).
- ¹⁵M.-R. Pendar and J. C. Páscoa, "Numerical modeling of the distribution of virus carrying saliva droplets during sneeze and cough," *Phys. Fluids* **32**(8), 083305 (2020).
- ¹⁶B. Wang, H. Wu, and X.-F. Wan, "Transport and fate of human expiratory droplets—A modeling approach," *Phys. Fluids* **32**(8), 083307 (2020).
- ¹⁷H. De-Leon and F. Pederiva, "Particle modeling of the spreading of coronavirus disease (COVID-19)," *Phys. Fluids* **32**(8), 087113 (2020).
- ¹⁸S. Verma, M. Dhanak, and J. Frankenfield, "Visualizing droplet dispersal for face shields and masks with exhalation valves," *Phys. Fluids* **32**(9), 091701 (2020).
- ¹⁹E. Hossain, S. Bhadra, H. Jain, S. Das, A. Bhattacharya, S. Ghosh, and D. Levine, "Recharging and rejuvenation of decontaminated N95 masks," *Phys. Fluids* **32**(9), 093304 (2020).
- ²⁰M. Vadivukkarasan, K. Dhivayaraja, and M. V. Panchagnula, "Breakup morphology of expelled respiratory liquid: From the perspective of hydrodynamic instabilities," *Phys. Fluids* **32**(9), 094101 (2020).
- ²¹S. K. Das, J.-E. Alam, S. Plumari, and V. Greco, "Transmission of airborne virus through sneezed and coughed droplets," *Phys. Fluids* **32**(9), 097102 (2020).
- ²²R. B. Bird, C. F. Curtiss, R. C. Armstrong, and O. Hassager, *Dynamics of Polymeric Liquids*, 2nd ed. (John Wiley & Sons, Inc., New York, 1987), Vol. 2.
- ²³W. Zhang, N. H. Olson, T. S. Baker, L. Faulkner, M. Agbandje-McKenna, M. I. Boulton, J. W. Davies, and R. McKenna, "Structure of the maize streak virus geminate particle," *Virology* **279**(2), 471–477 (2001).
- ²⁴D. L. D. Caspar and A. Klug, "Physical principles in the construction of regular viruses," in *Cold Spring Harbor Symposia on Quantitative Biology* (Cold Spring Harbor Laboratory Press, Long Island, NY, 1962), Vol. 27, pp. 1–24.
- ²⁵D. J. Wales and S. Ulker, "Structure and dynamics of spherical crystals characterized for the Thomson problem," *Phys. Rev. B* **74**(21), 212101 (2006).
- ²⁶D. J. Wales, H. McKay, and E. L. Altschuler, "Defect motifs for spherical topologies," *Phys. Rev. B* **79**(22), 224115 (2009).
- ²⁷O. Hassager, "On the kinetic theory and rheology of multibead models for macromolecules," Ph.D. thesis, Chemical Engineering Department, University of Wisconsin, Madison, USA, June 18, 1973.
- ²⁸J. H. Piette, A. J. Giacomin, and M. A. Kanso, "Complex viscosity of helical and doubly helical polymeric liquids from general rigid bead-rod theory," *Phys. Fluids* **31**(11), 111904 (2019), Feature article.
- ²⁹M. A. Kanso, "Polymeric liquid behavior in oscillatory shear flow," M.S. thesis, Polymers Research Group, Chemical Engineering Department, Queen's University, Kingston, Canada, July 23, 2019.
- ³⁰O. Hassager, "Kinetic theory and rheology of bead-rod models for macromolecular solutions. II. Linear unsteady flow properties," *J. Chem. Phys.* **60**(10), 4001–4008 (1974).
- ³¹M. A. Kanso, A. J. Giacomin, C. Saengow, and J. H. Piette, "Macromolecular architecture and complex viscosity," *Phys. Fluids* **31**(8), 087107 (2019), Editor's pick.
- ³²M. A. Kanso and A. J. Giacomin, "Van Gurp-Palmen relations for long-chain branching from general rigid bead-rod theory," *Phys. Fluids* **32**(3), 033101 (2020).
- ³³M. A. Kanso, A. J. Giacomin, C. Saengow, and J. H. Piette, "Diblock copolymer architecture and complex viscosity," *Int. J. Mod. Phys. B* **34**(14n16), 2040110 (2020).
- ³⁴M. A. Kanso and A. J. Giacomin, "Polymer branching and first normal stress differences in small-amplitude oscillatory shear flow," *Can. J. Chem. Eng.* **98**(7), 1444–1455 (2020).
- ³⁵R. B. Bird, O. Hassager, R. C. Armstrong, and C. F. Curtiss, *Dynamics of Polymeric Liquids*, 1st ed. (John Wiley and Sons, Inc., New York, 1977), Vol. 2.
- ³⁶M. A. Kanso, L. M. Jbara, A. J. Giacomin, C. Saengow, and P. H. Gilbert, "Order in polymeric liquids under oscillatory shear flow," *Phys. Fluids* **31**(3), 033103 (2019).
- ³⁷C. J. Oliver, K. F. Shortridge, and G. Belyanin, "Diffusion coefficient and molecular weight of type 5 adenovirus by photon-correlation spectroscopy," *Biochim. Biophys. Acta, Gen. Subj.* **437**(2), 589–598 (1976).
- ³⁸T. A. King, A. Knox, and J. D. G. McAdam, "Translational and rotational diffusion of tobacco mosaic virus from polarized and depolarized light scattering," *Biopolymers* **12**(8), 1917–1926 (1973).
- ³⁹D. Lehner, H. Lindner, and O. Glatter, "Determination of the translational and rotational diffusion coefficients of rodlike particles using depolarized dynamic light scattering," *Langmuir* **16**(4), 1689–1695 (2000).
- ⁴⁰A. Wada, N. C. Ford, Jr., and F. E. Karasz, "Rotational diffusion of tobacco mosaic virus," *J. Chem. Phys.* **55**(4), 1798–1802 (1971).
- ⁴¹H. Z. Cummins, F. D. Carlson, T. J. Herbert, and G. Woods, "Translational and rotational diffusion constants of tobacco mosaic virus from Rayleigh linewidths," *Biophys. J.* **9**(4), 518–546 (1969).
- ⁴²C. T. O'Konski and A. J. Haltner, "Characterization of the monomer and dimer of tobacco mosaic virus by transient electric birefringence¹," *J. Am. Chem. Soc.* **78**(15), 3604–3610 (1956).
- ⁴³H. Boedtker and N. S. Simmons, "The preparation and characterization of essentially uniform tobacco mosaic virus particles," *J. Am. Chem. Soc.* **80**(10), 2550–2556 (1958).
- ⁴⁴Q. Yao, P. S. Masters, and R. Ye, "Negatively charged residues in the endodomain are critical for specific assembly of spike protein into murine coronavirus," *Virology* **442**(1), 74–81 (2013).
- ⁴⁵R. Ye, C. Montalto-Morrison, and P. S. Masters, "Genetic analysis of determinants for spike glycoprotein assembly into murine coronavirus virions: Distinct roles for charge-rich and cysteine-rich regions of the endodomain," *J. Virol.* **78**(18), 9904–9917 (2004).
- ⁴⁶M. A. Tortorici and D. Veessler, "Structural insights into coronavirus entry," *Adv. Virus Res.* **105**, 93–116 (2019).
- ⁴⁷N. R. Eddy and J. N. Onuchic, "Rotation-activated and cooperative zipping characterize class I viral fusion protein dynamics," *Biophys. J.* **114**(8), 1878–1888 (2018).
- ⁴⁸W. E. Stewart and J. P. Sørensen, "Hydrodynamic interaction effects in rigid dumbbell suspensions. II. Computations for steady shear flow," *Trans. Soc. Rheol.* **16**(1), 1–13 (1972).
- ⁴⁹J. H. Piette, L. M. Jbara, C. Saengow, and A. J. Giacomin, "Exact coefficients for rigid dumbbell suspensions for steady shear flow material function expansions," *Phys. Fluids* **31**(2), 021212 (2019).
- ⁵⁰L. G. Leal and E. J. Hinch, "The rheology of a suspension of nearly spherical particles subject to Brownian rotations," *J. Fluid Mech.* **55**(4), 745–765 (1972).
- ⁵¹SolidWorks (Version 2019 sp4), Dassault Systèmes SolidWorks Corporation, Waltham, MA, 2019.
- ⁵²R. B. Bird and A. J. Giacomin, "Who conceived the 'complex viscosity'?", *Rheol. Acta* **51**(6), 481–486 (2012).
- ⁵³A. J. Giacomin and R. B. Bird, "Erratum: Official nomenclature of The Society of Rheology: $-\eta'$," *J. Rheol.* **55**(4), 921–923 (2011).
- ⁵⁴J. D. Ferry, *Viscoelastic Properties of Polymers*, 3rd ed. (John Wiley & Sons, New York, 1980).

- ⁵⁵R. B. Bird, R. C. Armstrong, and O. Hassager, *Dynamics of Polymeric Liquids*, 1st ed. (Wiley, New York, 1977), Vol. 1.
- ⁵⁶J. Atabekov, N. Nikitin, M. Arkhipenko, S. Chirkov, and O. Karpova, "Thermal transition of native tobacco mosaic virus and RNA-free viral proteins into spherical nanoparticles," *J. Gen. Virol.* **92**(2), 453–456 (2011).
- ⁵⁷N. Nemoto, J. L. Schrag, J. D. Ferry, and R. W. Fulton, "Infinite-dilution viscoelastic properties of tobacco mosaic virus," *Biopolymers* **14**(2), 409–417 (1975).
- ⁵⁸R. W. Horne, S. Brenner, A. P. Waterson, and P. Wildy, "The icosahedral form of an adenovirus," *J. Mol. Biol.* **1**, 84–86 (1959).
- ⁵⁹L. Franqueville, P. Henning, M. Magnusson, E. Vigne, G. Schoehn, M. E. Blair-Zajdel, N. Habib, L. Lindholm, G. E. Blair, S. S. Hong, and P. Boulanger, "Protein crystals in adenovirus type 5-infected cells: Requirements for intranuclear crystallogenesis, structural and functional analysis," *PLoS One* **3**(8), e2894 (2008).
- ⁶⁰B. W. Neuman, G. Kiss, A. H. Kunding, D. Bhella, M. F. Baksh, S. Connelly, B. Droese, J. P. Klaus, S. Makino, S. G. Sawicki, S. G. Siddell, D. G. Stamou, I. A. Wilson, P. Kuhn, and M. J. Buchmeier "A structural analysis of M protein in coronavirus assembly and morphology," *J. Struct. Biol.* **174**(1), 11–22 (2011).
- ⁶¹R. N. Kirchdoerfer, N. Wang, J. Pallesen, D. Wrapp, H. L. Turner, C. A. Cottrell, K. S. Corbett, B. S. Graham, J. S. McLellan, and A. B. Ward, "Stabilized coronavirus spikes are resistant to conformational changes induced by receptor recognition or proteolysis," *Sci. Rep.* **8**(1), 15701 (2018).
- ⁶²T. Keef and R. Twarock, "Affine extensions of the icosahedral group with applications to the three-dimensional organisation of simple viruses," *J. Math. Biol.* **59**(3), 287–313 (2009).
- ⁶³W. Song, M. Gui, X. Wang, and Y. Xiang, "Cryo-EM structure of the SARS coronavirus spike glycoprotein in complex with its host cell receptor ACE2," *PLoS Pathog.* **14**(8), 1007236 (2018).
- ⁶⁴N. Zhu, D. Zhang, W. Wang, X. Li, B. Yang, J. Song, X. Zhao, B. Huang, W. Shi, R. Lu, P. Niu, F. Zhan *et al.*, "A novel coronavirus from patients with pneumonia in China, 2019," *N. Engl. J. Med.* **382**(8), 727–733 (2020).
- ⁶⁵E. M. Furst and T. M. Squires, *Microrheology* (Oxford University Press, Oxford, 2017).
- ⁶⁶X. Zhu, B. Kundukad, and J. R. C. Van der Maarel, "Viscoelasticity of entangled λ -phage DNA solutions," *J. Chem. Phys.* **129**(18), 185103 (2008).
- ⁶⁷J. R. Van der Maarel, *Introduction to Biopolymer Physics* (World Scientific Publishing Company, 2007).
- ⁶⁸C. S. Goldsmith, K. M. Tatti, T. G. Ksiazek, P. E. Rollin, J. A. Comer, W. W. Lee, P. A. Rota, B. Bankamp, W. J. Bellini, and S. R. Zaki, "Ultrastructural characterization of SARS coronavirus," *Emerging Infect. Dis.* **10**(2), 320–326 (2004).